




Erratum: Confined vortices in de facto mesoscopic $\text{Mo}_{80}\text{Ge}_{20}$ disks with sector defects (2018 *Supercond. Sci. Technol.* **31** 125009)

The Dang Vu^{1,2}, Ho Thanh Huy^{1,2}, Atsuki Ito¹, Masaki Toji¹, Hiroaki Shishido^{1,3}, Masaru Kato^{1,3,4}, Masahiko Hayashi⁵ and Takekazu Ishida^{3,6} 

¹ Department of Physics and Electronics, Osaka Prefecture University, 1-1 Gakuen-cho, Naka-ku, Sakai, Osaka 599-8531, Japan

² Department of Physics and Electronics, University of Sciences, Vietnam National University HCMC, 227 Nguyen Van Cu, District 5, Ho Chi Minh City, Vietnam

³ NanoSquare Research Institute, Osaka Prefecture University, 1-1 Gakuen-cho, Naka-ku, Sakai, Osaka 599-8531, Japan

⁴ Department of Mathematical Sciences, Osaka Prefecture University, 1-1 Gakuen-cho, Naka-ku, Sakai, Osaka 599-8531, Japan

⁵ Faculty of Education and Human Studies, Akita University, 1-1 Tegata Gakuen-machi, Akita-shi, Akita 010-8502, Japan

⁶ Quantum and Radiation Engineering, Osaka Prefecture University, 1-2 Gakuen-cho, Naka-ku, Sakai, Osaka 599-8570, Japan

E-mail: ishida@center.osakafu-u.ac.jp

(Some figures may appear in colour only in the online journal)

During the conversion of the graphics in the production process, some data in the x axes labels were lost in figures 4(i) and (k). The complete version of figure 4 is given below.

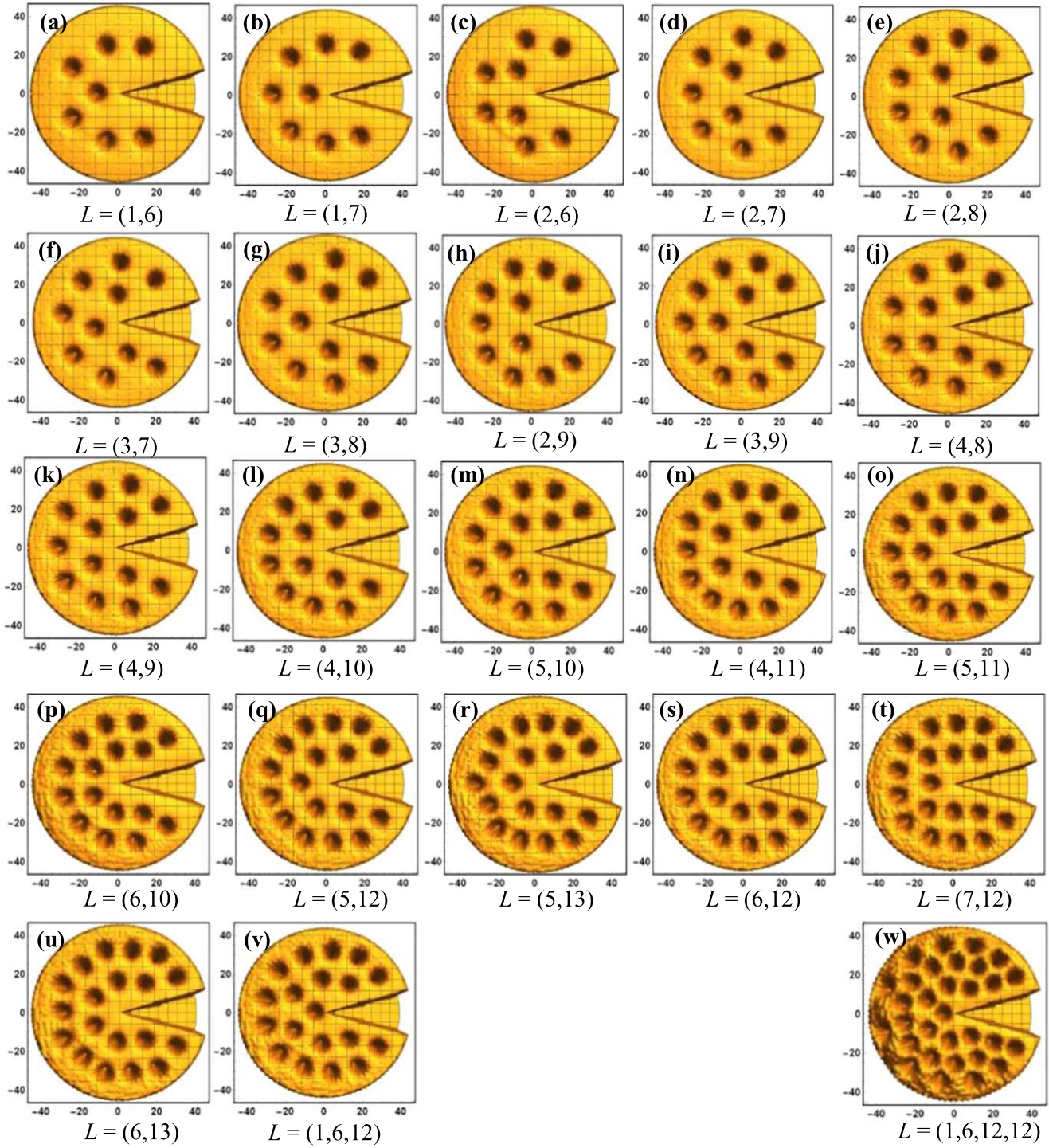




Figure 4. Vortex distribution in a superconducting circular disk with a sector defect of opening angle 30° showing multiple-arc structures with a circumradius of $R = \lambda$ and a GL parameter of $\kappa = 45$ represented in terms of the spatial distribution of the amplitude of the order parameter Δ under various different external fields (a) $h = 0.0030$, (b) $h = 0.0024$, (c) $h = 0.0024$, (d) $h = 0.0026$, (e) $h = 0.0033$, (f) $h = 0.0032$, (g) $h = 0.0034$, (h) $h = 0.0037$, (i) $h = 0.0037$, (j) $h = 0.0035$, (k) $h = 0.0038$, (l) $h = 0.0044$, (m) $h = 0.0043$, (n) $h = 0.0046$, (o) $h = 0.0045$, (p) $h = 0.0055$, (q) $h = 0.0050$, (r) $h = 0.0056$, (s) $h = 0.0050$, (t) $h = 0.0059$, (u) $h = 0.0053$, (v) $h = 0.0054$, (w) $h = 0.0099$.

ORCID iDs

Takekazu Ishida  <https://orcid.org/0000-0002-9629-5178>

Confined vortices in *de facto* mesoscopic $\text{Mo}_{80}\text{Ge}_{20}$ disks with sector defects

The Dang Vu^{1,2}, Ho Thanh Huy^{1,2}, Atsuki Ito¹, Masaki Toji¹,
Hiroaki Shishido^{1,3}, Masaru Kato^{1,3,4}, Masahiko Hayashi⁵  and
Takekazu Ishida^{3,6,7} 

¹ Department of Physics and Electronics, Osaka Prefecture University, 1-1 Gakuen-cho, Naka-ku, Sakai, Osaka 599-8531, Japan

² Department of Physics and Electronics, University of Sciences, Vietnam National University HCMC, 227 Nguyen Van Cu, District 5, Ho Chi Minh City, Vietnam

³ NanoSquare Research Institute, Osaka Prefecture University, 1-1 Gakuen-cho, Naka-ku, Sakai, Osaka 599-8531, Japan

⁴ Department of Mathematical Sciences, Osaka Prefecture University, 1-1 Gakuen-cho, Naka-ku, Sakai, Osaka 599-8531, Japan

⁵ Faculty of Education and Human Studies, Akita University, 1-1 Tegata Gakuen-machi, Akita-shi, Akita 010-8502, Japan

⁶ Quantum and Radiation Engineering, Osaka Prefecture University, 1-2 Gakuen-cho, Naka-ku, Sakai, Osaka 599-8570, Japan

E-mail: ishida@center.osakafu-u.ac.jp

Received 25 July 2018, revised 27 September 2018

Accepted for publication 28 September 2018

Published 2 November 2018



Abstract

We introduce a sectoral defect into a disk (creating a Pac-ManTM-shaped plate) to investigate effect of the symmetry breaking of a perfect disk on vortex dynamics. The sectoral defect acts as a preferential gateway for vortices to enter the disk. Vortices tend to form a symmetric configuration with respect to the mirror-symmetry line under various different applied magnetic fields. We found that the vortex configuration of the Pac-ManTM-shaped disk exhibits an exotic arc structure, in contrast to the well-known shell structure of a disk. A characteristic of the vortex configuration is the critical number of vortices (or ‘magic number’) at which the single-arc structure becomes a multiple-arc structure, which can be tuned by changing the opening angle of the sectoral defect. We also noticed by comparing the free energies of the vortex distributions, that there are several competing metastable states with the same number of vortices when the ratio of the number of vortices in the outer arc to the number in the inner arc approaches two, for which stable triangular clusters might form part of the configurations. We conclude that there are reasonable agreements between the Ginzburg–Landau calculations and experimental scanning SQUID microscope images of vortices in *de facto* mesoscopic Pac-ManTM-shaped $\text{Mo}_{80}\text{Ge}_{20}$ thin disks.

Keywords: mesoscopic superconductor, vortex distribution, SQUID microscopy, Ginzburg–Landau calculations, filling rule

(Some figures may appear in colour only in the online journal)

1. Introduction

In superconducting disks of a size comparable to the magnetic penetration depth λ , vortices are confined to a limited regime

by Meissner shielding currents and the geometrical boundary. The size requirements for satisfying the mesoscopic nature can be relaxed by thinning a superconducting film so that Pearl vortices are evident, exhibiting a long effective penetration depth. Vortices in mesoscopic systems differ from those in bulk superconductors and tend to form a particular

⁷ Author to whom any correspondence should be addressed.

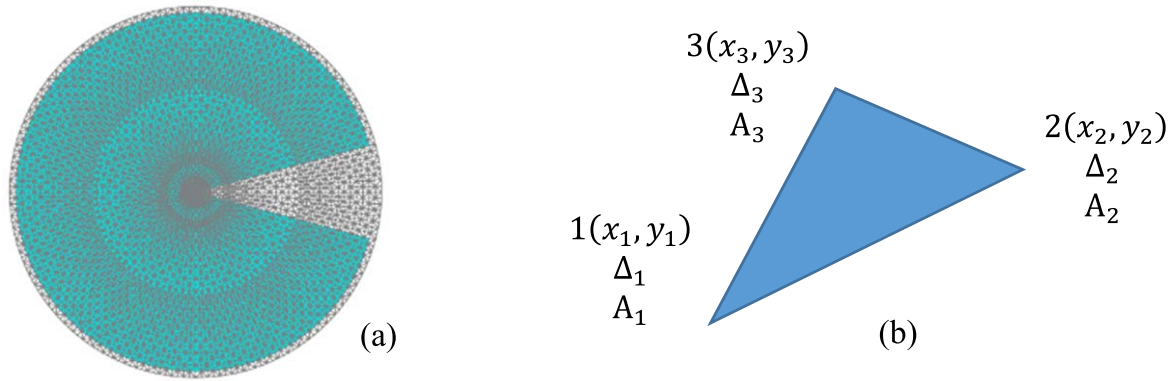


Figure 1. (a) Division of a circular superconductor with a sector defect into triangular elements in the finite element method. (b) Definition of the order parameter Δ_i and magnetic vector potential A_i at each node of a triangular element.

configuration due to vortex–vortex repulsion, boundary–vortex interactions, and vortex-shielding-current interactions. Such vortex configurations exhibit interesting exotic features depending on the pattern geometry, external magnetic field, and number of vortices [1–5]. The vortex profiles in symmetric geometries have been thoroughly investigated for several typical symmetric systems such as circles and regular polygons. It has been found, for instance, that the geometrical boundary plays a crucial role in creating a shell structure like an artificial atom of vortices [2, 6, 7]. The boundary conditions tend to impose a particular vortex arrangement in non-circular plates such as an equilateral triangle (C_3) [8, 9], and a square C_4 symmetry [10, 11]. Multiple-shell structures in small disks [5, 12] exhibit a vortex filling rule which is dependent on the shape of the plates. Complex vortex configurations have been observed by introducing an artificial pin [1] and a regular concave decagon plate or a star-shaped plate into a film [13, 14]. Vortices in a type II-superconducting plate sense potential barriers upon entering the interior of the plate, and are influenced by vortex–vortex interactions, the confinement provided by the Meissner shielding currents [15, 16], the Bean–Livingston surface barrier, surface roughness, and defects at the interface [17, 18]. We considered that a defect may cause a local lowering of the surface barrier when a vortex enters a superconductor [19–21]. Alstrøm *et al* [22] investigated the dynamics of vortices entering a sample for increasing applied magnetic fields when a small triangular defect is introduced at the edge of a circular disk, using the time dependent Ginzburg–Landau equation. The number of confined vortices in the plate increased as the applied magnetic field increased, regardless of the presence of the surface defects [17, 18].

In this study, we present theoretical predictions and experimental observations of the exotic vortex distribution in a circular disk with a sector defect (or a Pac-Man⁸-like shape). Our goal is to pursue for a filling rule based on the theoretically generated images of vortex configurations as this will allow theoretical comparisons to be conducted more systematically than would be the case for the time-consuming method of obtaining experimental images.

2. Numerical results

We carried out Ginzburg–Landau (GL) calculations using the finite element method [1, 23]. Due to limitations in our computational resources, we considered only a realistic physical parameter for the penetration depth λ in the GL calculations with a coherence length ξ set artificially large enough compared to the realistic physical parameters of superconducting $\text{Mo}_{80}\text{Ge}_{20}$. We believe that this is appropriate for studying vortex configurations because the vortex configurations are primarily determined by the magnetic interaction between vortices, whereas λ is the most important parameter defining the vortex states. We represent the theoretical vortex images in the Pac-Man-like plate in terms of the amplitude of an order parameter. We recognize that the theoretical images are not strictly physically justified, but it is convenient to generate a vortex distribution visually using an overly long ξ in our theoretical calculations. Accordingly, the GL parameter κ is also not physically accurate in our calculations, but it does not affect the essential features of our *de facto* mesoscopic systems.

Figure 1(a) shows the division of a circular superconductor with a sector defect into triangular elements in the finite element method. At each node of a triangular element, the values of an order parameter Δ_i and a magnetic vector potential A_i are defined as shown in figure 1(b). The finite element method is useful for the arbitrary-shaped geometry in our calculations. As shown in figures 2–4, we calculated vortex configurations in a Pac-Man-shaped plate with a GL parameter of $\kappa = 45$ and a circumradius of $R = \lambda$ to obtain *single-arc* and *higher-multiple-arc* structures at higher fields. We chose opening angles of the sector defect of 30° and 90° to control the vortex distribution in the multiple arcs. Our experiments are usually performed at $T = 4$ K, so we set a reduced temperature of $T/T_c = 0.5$ in our numerical calculations. The magnetic field is applied perpendicular to the Pac-Man-shaped plate. The normalized magnetic field $h = H/H_{c2}$ is a reduced magnetic field representing the applied magnetic field H in units of the upper critical field H_{c2} . The magnetic field H ranges up to 10.5% of H_{c2} . Figure 2 shows an arc-shaped vortex distribution in a superconducting circular disk with a sector defect with an opening

⁸ Pac-Man is a trademark of Bandai Namco Entertainment Inc.

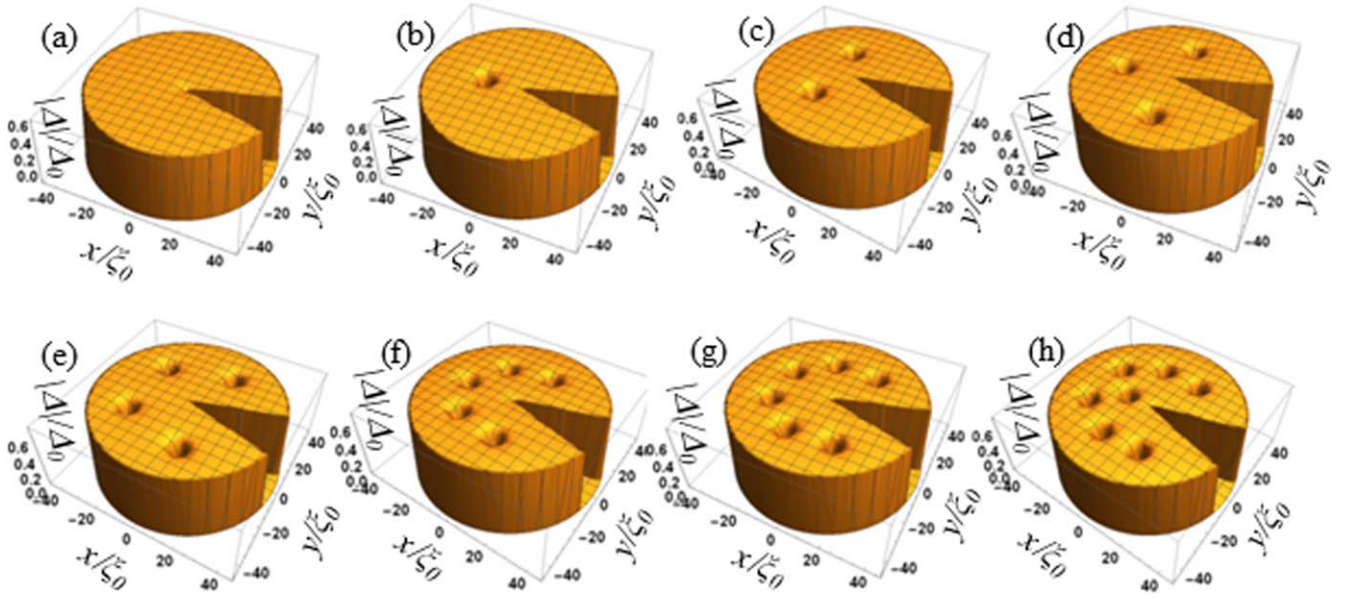


Figure 2. Vortex distribution in a superconducting circular disk with a sector defect of opening angle 30° with a circumradius of $R = \lambda$ and a GL parameter of $\kappa = 45$ in terms of the spatial distribution of the amplitude of the order parameter Δ under various different external fields (a) $h = 0.007$, (b) $h = 0.0011$, (c) $h = 0.0010$, (d) $h = 0.0013$, (e) $h = 0.0018$, (f) $h = 0.0023$, (g) $h = 0.0022$, (h) $h = 0.0030$.

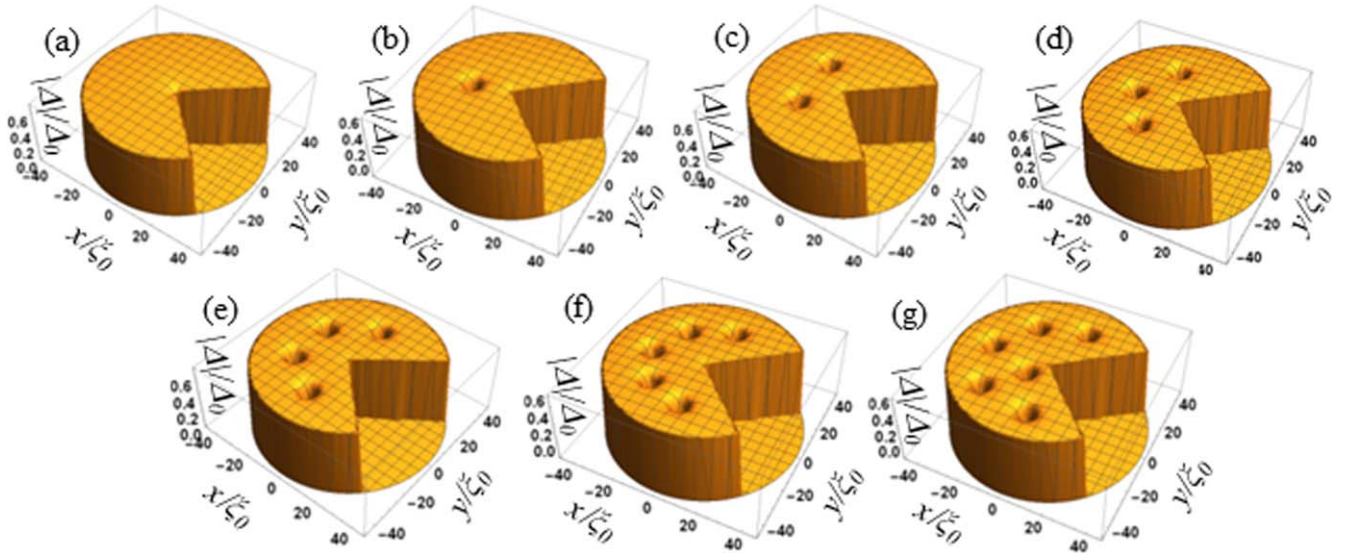


Figure 3. Vortex distribution in a superconducting circular disk with a sector defect of opening angle 90° with a circumradius of $R = \lambda$ and a GL parameter of $\kappa = 45$ in terms of the spatial distribution of the amplitude of the order parameter Δ under various different external fields (a) $h = 0.0017$, (b) $h = 0.00192$, (c) $h = 0.00194$, (d) $h = 0.00232$, (e) $h = 0.00235$, (f) $h = 0.0024$, (g) $h = 0.0027$.

angle of 30° , where a circumradius of $R = \lambda$ and a GL parameter of $\kappa = 45$ were used. We show the spatial distribution of vortices in terms of the amplitude of the order parameter Δ under various external fields. Figure 3 shows an arc-shaped vortex distribution in a superconducting circular disk in terms of the amplitude of the order parameter Δ with a sector defect with an opening angle of 90° for a circumradius of $R = \lambda$ and a GL parameter of $\kappa = 45$.

We first focus on the vortex configuration in a single-arc structure. As the magnetic field is increased the vortex state evolves as follows: (1) the Meissner state appears, as shown in figures 2(a) and 3(a). Since the tip of the defect sits at the center of circle, a valley of concaved area condenses the

magnetic flux lines expelled from the interior of the superconducting plate due to the superconducting diamagnetism. The magnetic field is highest at the tip of the sector defect and the enhanced magnetic pressure works to promote field penetration through the tip of the defect into the Pac-Man-shaped plate. We consider that this causes a local lowering of the surface barrier, and hence the defect acts as a gate for vortices to enter the sample. As noted by Baelus *et al* [17], the Cooper pair density around a surface defect decreases as the applied magnetic field increases. This leads to the appearance of a vortex inside the plate. According to Alstrøm *et al* [22], the energy barrier at the boundary is the lowest at the sectoral defect of the disk, and therefore vortices prefer to enter the

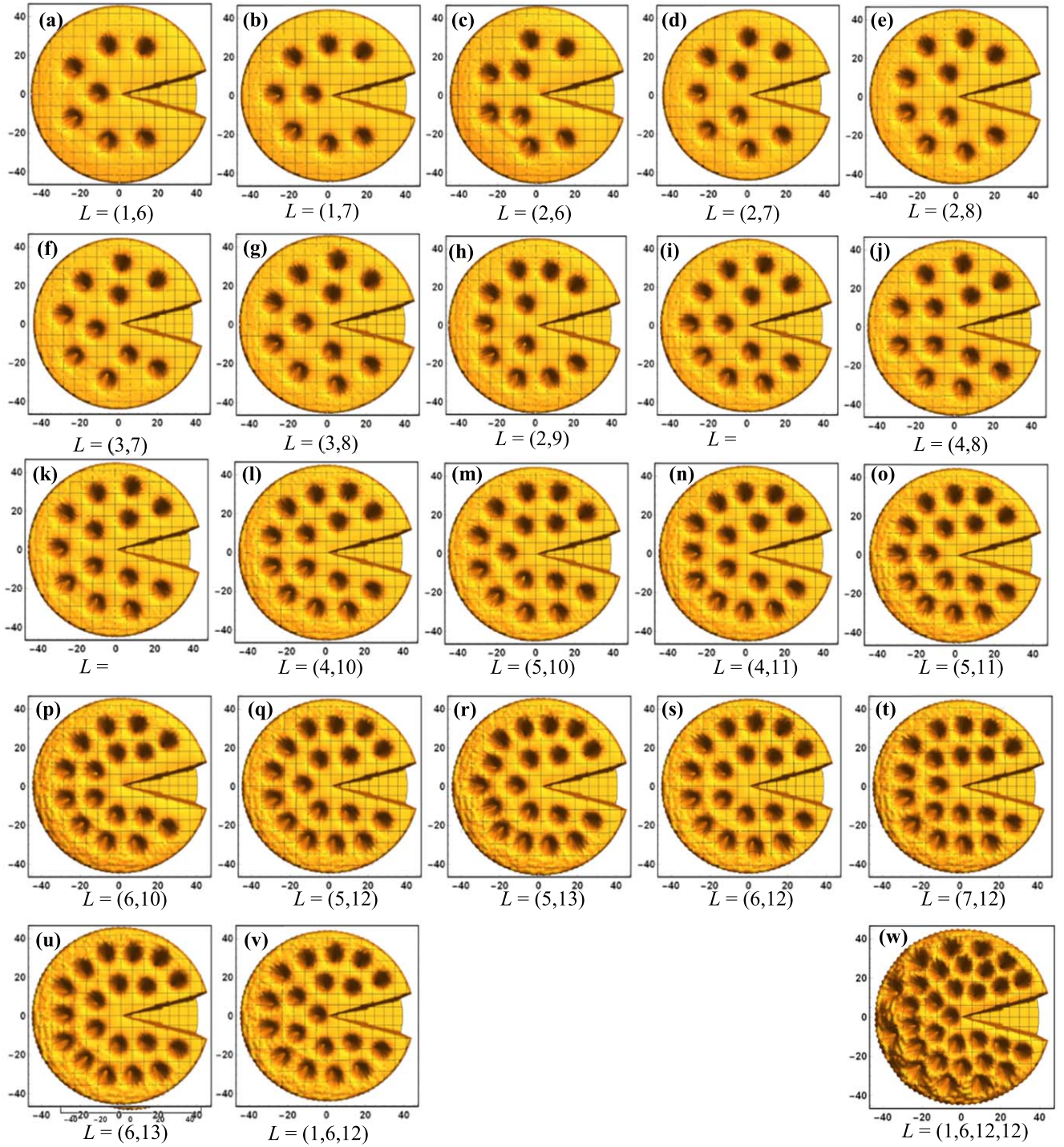


Figure 4. Vortex distribution in a superconducting circular disk with a sector defect of opening angle 30° showing multiple-arc structures with a circumradius of $R = \lambda$ and a GL parameter of $\kappa = 45$ represented in terms of the spatial distribution of the amplitude of the order parameter Δ under various different external fields (a) $h = 0.0030$, (b) $h = 0.0024$, (c) $h = 0.0024$, (d) $h = 0.0026$, (e) $h = 0.0033$, (f) $h = 0.0032$, (g) $h = 0.0034$, (h) $h = 0.0037$, (i) $h = 0.0037$, (j) $h = 0.0035$, (k) $h = 0.0038$, (l) $h = 0.0044$, (m) $h = 0.0043$, (n) $h = 0.0046$, (o) $h = 0.0045$, (p) $h = 0.0055$, (q) $h = 0.0050$, (r) $h = 0.0056$, (s) $h = 0.0050$, (t) $h = 0.0059$, (u) $h = 0.0053$, (v) $h = 0.0054$, (w) $h = 0.0099$.

superconducting disk through this defect. (2) The first vortex appears inside the disk from the tip of the defect along the mirror-symmetry line of the Pac-Man-shaped plate (see figures 2(b), 3(b)). (3) The second vortex also enters the disk through the defect. When there are two vortices, they do not sit on the mirror-symmetry line, but rather take symmetrical

positions with respect to the mirror-symmetry line (see figures 2(c), 3(c)), with their positions determined by the balance of vortex–vortex repulsion, the vortex–boundary interaction, and the confinement by the Meissner shielding currents. The Meissner shielding currents should be strongest near the tip of the sectoral defect because the external

magnetic flux is highly condensed in the region of the sectoral defect. The most stable configuration is shown in figures 2(c) and 3(c), namely the tip of the defect and the two vortices form a triangle. According to Baelus *et al* [17], the vortices interact with the tip of defect and are rotated by $\pi/2$ to make metastable states such that they lie along the circumference perpendicular to the defect. As noted by Ho *et al* [24] and Kokubo *et al* [2], the circular plate has a single rotational degree of freedom in the vortex configuration. In contrast, a perfect disk has infinite degrees of freedom in rotational symmetry. (4) The third, fourth, and fifth vortices join to form an exotic configuration in an arc shape. When there is an odd number of vortices (which we will hereafter refer to as the vorticity, L), one vortex sits on the mirror-symmetry line while the other vortices are equally located on both sides of the mirror-symmetry line. For an even vorticity no vortices sit on the mirror-symmetry line (see figures 2(c), (e), (g), 3(c), (e)). The vorticity where the vortex pattern transitions from a single-arc configuration to a multi-arc configuration is dependent on the opening angle of the sector defect. We denote this vorticity as the magic number for the arc structure. According to our numerical studies, the magic number for an opening angle of 30° is six and for an opening angle of 90° it is five (see figures 2(h), 3(g)). The area that can accommodate vortices is smaller when the Pac-Man-shaped disk opens its mouth wider. Kokubo *et al* [2] and Grigorieva *et al* [12] noted that the maximum vorticity of a single shell in a circular disk is fixed at five. However, the single-arc profile of a Pac-Man-shaped plate is different from that of the perfect disk. The presence of a defect increases the radius of the vortex ring compared to that in a perfect disk as it pushes the vortex ring into the surrounding area. Thus, we find that the nature of a vortex configuration in a perfect disk is modified to be *exotic* by the presence of a sector defect in the Pac-Man-like plate. We found therefore that the defect as an artificial element plays a crucial role in modifying the vortex structure from that of the circular disk and that the vortex configuration can be adjusted by tuning the opening angle of the sector defect. Braverman *et al* [25] reported a related theoretical study, where short-range columnar defects introduced into a mesoscopic superconducting disk destroy a rotational symmetry of vortex configurations in the disk.

We also investigated multiple arc configurations of vortices in Pac-Man-shaped plates with open defects of angles 30° and 90° . The evolution of the vortex images in a double-arc structure for an opening angle 30° of the sector defect is shown in figure 4. Table 1 shows the free energy calculations of the vortex configurations in a double-arc structure to compare their stability with regard to the free energy of the vortex system. The vortex distribution evolves with an increase of the applied magnetic field as follows: (1) at $L = 7$, one vortex is nucleated in the plate near the tip while the others form an arc-shaped or C-shaped structure in the outer area (see figure 4(a)), which is the beginning of a double-arc structure. Following standard notation used for a perfect disk, the vorticity can be expressed as $(N_i, N_o) = (1, 6)$, where N_i is the inner-arc vorticity and N_o is the outer-arc vorticity. We note that a Pac-Man-shaped plate with an opening angle of

Table 1. Evolution of vorticity L with the different vortex configurations in multiple arc structures in a Pac-Man-shaped plate with a sector defect of opening angle 30° with a circumradius of $R = \lambda$ and a GL parameter of $\kappa = 45$. We also compare the free energies obtained by the GL calculations in arbitrary units.

Vorticity L	Vortex configurations	Free energy
7	(1, 6)	212.8
8	(1, 7)	215.6
	(2, 6)	215.0
9	(2, 7)	247.4
10	(2, 8)	307.7
	(3, 7)	303.1
11	(2, 9)	357.3
	(3, 8)	339.5
12	(3, 9)	383.8
	(4, 8)	372.2
13	(4, 9)	416.9
14	(4, 10)	485.9
15	(4, 11)	529.0
	(5, 10)	506.4
16	(5, 11)	580.8
	(6, 10)	626.9
17	(5, 12)	617.2
18	(5, 13)	696.2
	(6, 12)	643.9
19	(6, 13)	709.5
	(7, 12)	750.6
	(1, 6, 12)	704.6
20	(1, 6, 13)	759.2

90° starts to form a double-arc structure of (1, 5) (see figure 3(g)). The appearance of a vortex in an inner arc expands the radius of the outer arc, where the vortex–vortex distance is somewhat wider than that in the inner arc. Therefore, further additional vortices have to find stable states within the competing interactions among the inner vortices, outer vortices, and confinement supercurrents around the boundary. We see evidence of the interaction between an inner vortex and outer vortices in figure 4(a), where a wider spacing is observed between vortices near the mirror-symmetry line than between the vortices in the outer arc. In figure 3(g), it appears that an inner vortex applies a force to a neighboring outer-arc vortex, which was originally located on the mirror-symmetry line for $L = 5$ in figure 3(f), and the inner vortex of figure 3(g) is also not located on the mirror-symmetry line of the sector defect. (2) As the applied magnetic field is increased, the vorticity increases to $L = 8$. The order parameter for this applied magnetic field is $h = 0.0024$. In this case, two different vortex configurations (1, 7) and (2, 6) can appear, as shown in figures 4(b) and (c). The vortex configuration of (1, 7) can be explained as follows. The eighth vortex interacts with the existing inner vortex influenced by the flowing conditions of the boundary supercurrents and highly dense magnetic flux around the tip of the defect outside the plate, and one vortex is forced into the outer arc with a weak interaction. However, the difference in vorticity between the inner and outer arcs is likely to cause an instability in the vortex distribution. We consider that the

vortex distribution of (2, 6) is more stable than the vortex distribution of (1, 7), due to the slightly lower free energy of the local stable structure of 215.0 for (2, 6) than that of 215.6 for (1, 7) in our calculations. In the case of $L = (2, 6)$, the interaction between the inner and outer vortices expands the space between some of the vortices in the outer arc. This means that the vortex–vortex repulsion in the outer arc is weaker than the confinement pressure of the shielding currents induced by the highly dense magnetic flux outside the tip. (3) If a new vortex enters the inner arc through the defect, the vorticity becomes $L = 9$ to form a double-arc distribution of $L = (2, 7)$, as shown in figure 4(d). Each of the two inner vortices act to divide the outer-arc vortices into three groups (2-3-2). The combination of two inner vortices and seven outer vortices forms a good symmetric configuration with respect to the mirror-symmetry line of the Pac-Man-shaped plate. (4) The vorticity evolves further with an increase in the applied magnetic field. The inner vortices try to form a C-shaped structure and tend to reproduce the filling rule of the single-arc distribution displayed in figure 2. We also found two different vortex configurations (2, 8) and (3, 7) for $L = 10$ (see figures 4(e) and (f)) and (3, 8) and (2, 9) for $L = 11$ (see figures 4(g) and (h)). The vortex configuration of $L = (2, 8)$ has a free energy of 307.7 while that for the configuration $L = (3, 7)$ is 303.1. The vortex configuration of $L = (2, 9)$ has a free energy of 357.3 while that for $L = (3, 8)$ is 339.5. We consider that there are competing interactions leading to different vortex states, of which the system energies are very similar. The vortex distributions (3, 7) and (3, 8) are not truly stable but are metastable. Moreover, it should be noted that the experimental observations do not always recover the true minimum state realized in numerical calculations. We surmise that we often observe the metastable states in experimental observations. We find that a similar situation continues for further increases in the applied magnetic field, as systematically shown in figures 4(i)–(v). However, the difference in vortex–vortex spaces is no longer sufficiently clear to classify the distribution when L is greater than 20. We also find that vortices in a Pac-Man-shaped plate tend to form a symmetric configuration with respect to the mirror-symmetry line of the sector defect.

In order to determine a rule for metastable configurations under the same vorticity, in table 1 we compare the vorticities, vortex configuration as (N_i, N_o) , and free energies. When the ratio N_o/N_i of the outer vorticity and inner vorticity is very close to two, one inner vortex tends to combine with two outer vortices to create a stable triad set of vortices in a triangular form and occupy a sector of the Pac-Man-shaped plate. (5) At $L = 19$ (1, 6, 12), a triple-arc structure appears for the first time as the magnetic field increases. We find that the maximum vorticity of the inner arc is close to six, which is the same as the magic number when there is a transition from a single-arc structure to a double-arc structure. The same interpretation applies in the case of the transition from a triple-arc structure to a quadruple-arc structure (see figure 4(w)). We also found that there is a critical number of five for the inner vorticity when a single-arc structure moves to a double-arc structure for an opening angle of 90° . Similarly, there is a

critical vorticity when it transfers from a double-arc structure to a triple-arc structure (see table 2). Comparing multiple-arc (shell) structures between a Pac-Man-shaped plate, a circular disk, and a square plate, we found that the maximum (critical) vorticity of the inner-arc (shell) structure depends on the geometry of the plate. For instance, as noted by Kokubo *et al* [2] and Grigorieva *et al* [12] for circular disks and by Kokubo *et al* [3] and Zhao *et al* [5] for square plates, the transition from a single-shell structure to a double-shell structure occurs at a vorticity of five for a disk and at four for a square. It is worth noting that the critical vorticity at the inter-arc transition from a single to a double arc or from a double to a triple arc for a Pac-Man-shaped plate can be controlled by tuning the opening angle of sector defect. We present a new finding that ‘a critical transient state from an N -ring configuration to an $(N + 1)$ -ring configuration can be controlled by the geometry of the Pac-Man-shaped plate.’ We also find that there are common vortex configurations between a Pac-Man-shaped plate, a square plate and a circular disk such as $L = (1, 6)$, $(1, 7)$, $(2, 8)$, $(3, 8)$, $(4, 9)$, etc (see table 2). We consider that there are several stable combinations of inner vortices and outer vortices upon increasing vorticity before experiencing a critical transient vortex state. We believe that the exotic vortex state profiles revealed by the present work might have applications for potential superconducting devices.

We consider that the main difference between the perfect disk and the disk with sector defect comes from a role of cut edge of the sector defect in the case of a small opening angle. The presence of the defect edge would push vortices on an arc to realize a closer packing of vortices along the arc by the confinement by the vortex–boundary interaction. The present work concluded the magic number of six at an opening angle of 30° and the magic number of five at an opening angle of 90° with a circumradius of $R = \lambda$ and a GL parameter of $\kappa = 45$. We also found the magic number of five at an opening angle of 60° and the magic number of five at an opening angle of 90° and the magic number of four at an opening angle of 180° with a different circumradius of $R = 2\lambda$ and a different GL parameter of $\kappa = 10$ from $R = \lambda$ and $\kappa = 45$ of the results of figures 2–4, tables 1 and 2. If an opening angle becomes 300° , we expect that a situation would be very similar to the case of an equilateral triangle plate, of which an arc structure is inconclusive to appear in the preceding works [8, 9]. Further systematic studies are needed to conclude a general filling rule of vortices into a disk with a sector defect of arbitrary opening angle.

In the following section we present experimental investigations of the novel vortex states in a circular $\text{Mo}_{80}\text{Ge}_{20}$ disk with a sector defect.

3. Experimental details

We used a standard lithographic method to fabricate circular $\text{Mo}_{80}\text{Ge}_{20}$ plates with a sector defect. The Pac-Man-shaped patterns were designed using a layout editor. An electron-beam-lithography apparatus (ELS-7500EX, Elionix) was then

Table 2. Comparison of multiple arc (shell) structures between the two Pac-Man-shaped plates with a circumradius of $R = \lambda$ and a GL parameter of $\kappa = 45$, a circular disk and a square plate.

Vorticity (L)	Configuration			
	Pac-Man (angle 30°)	Pac-Man (angle 90°)	Circular disk [2, 12]	Square plate [3, 5]
3	(3)	(3)	(3)	(3)
4	(4)	(4)	(4)	(4)
5	(5)	(5)	(5)	(1, 4)
6	(6)	(1, 5)	(1, 5)	(1, 5)
7	(1, 6)	(1, 6)	(1, 6)	(1, 6)
8	(1, 7); (2, 6)	(1, 7); (2, 6)	(1, 7)	(1, 7) [3] (2, 6) [5]
9	(2, 7)	(2, 7)	(2, 7)	(1, 8)
10	(2, 8); (3, 7)	(2, 8)	(2, 8)	(2, 8)
11	(3, 8); (2, 9)	(3, 8)	(3, 8)	(3, 8)
12	(3, 9); (4, 8)	(3, 9); (4, 8)	(3, 9)	(4, 8)
13	(4, 9)	(4, 9)	(3, 10) [2]; (4, 9)	(4, 9)
14	(4, 10)	(5, 9)	(5, 9)	(4, 10)
15	(5, 10); (4, 11)	(5, 10)	(5, 10)	(4, 11) [3] (3, 12) [5]
16	(5, 11); (6, 10)	(1, 5, 10); (6, 10)	(5, 11)	(4, 12)
17	(5, 12)	(1, 6, 10)	(5, 12) [2] (1, 5, 11) [12]	(1, 4, 12)
18	(5, 13); (6, 12)	(1, 6, 11)		(1, 5, 12)
19	(7, 12); (6, 13); (1, 6, 12)			
31	(1, 6, 12, 12)			

used to prepare a patterned-resist film on a silicon substrate. On top of this resist pattern, we deposited a $\text{Mo}_{80}\text{Ge}_{20}$ thin film of thickness 67 nm by a DC sputtering apparatus. Keeping the substrate temperature as low as possible during deposition was important to form an amorphous thin film, and a water cooled Cu substrate holder was used to minimize substrate temperature increases during deposition, with silver paste used to ensure good thermal contact between the Si substrate and Cu substrate holder. We employed a specific sputtering process procedure including natural cooling down processes during plasma cleaning of the substrate, pre-sputtering, and sputtering. A lift-off technique was used wherein a film sample was dipped in an organic solvent such as dimethyl sulfoxide and 1-methyl-2-pyrrolidone. The success rate of the lift-off processes was clearly improved by ultraviolet irradiation before immersing the sample into the solvent as well as by heating the samples while they were being dipped into the solvent. After the lift-off process, we obtained an array of Pac-Man-shaped $\text{Mo}_{80}\text{Ge}_{20}$ plates. To avoid mutual interactions between vortices in neighboring superconducting plates, the neighboring patterns were separated by 120 μm . Finally, we coated the patterns with a protective SiO_2 layer of approximately 100 nm thickness to prevent the patterns from scratching during scanning SQUID microscope (SSM) tip scanning in contact with the sample surface (see figure 5).

The material parameters of the superconducting $\text{Mo}_{80}\text{Ge}_{20}$ thin films are determined to be as follows: the critical temperature of a $\text{Mo}_{80}\text{Ge}_{20}$ superconductor T_c is about 7 K. From $H_{c2}(0)$ at $T = 0$ K, we estimated the coherence length to be $\xi(0) = \sqrt{\Phi_0/2\pi H_{c2}(0)} = 5.25$ nm for $\text{Mo}_{80}\text{Ge}_{20}$ films.

The penetration depth $\lambda(0)$ is cited in the literature to be 0.58 μm at $T = 0$ K [2]. The thickness d of the thin film was chosen to be much smaller than the penetration depth so that the penetration depth is effectively lengthened to fulfill the relation $\lambda_{\text{eff}}(0) = 2\lambda^2(0)/d \gg \lambda(0)$ [26]. We designed our Pac-Man-shaped plate to have a diameter of $D = 85$ μm . The relation $R \sim 4.5\lambda_{\text{eff}}(0)$ makes it possible to classify our samples as *de facto* mesoscopic plates even if the actual size of the plate extends to the order of tens of μm . The distribution of vortices was observed directly by a commercial SSM (SQM-2000, Seiko Instruments) with a single-turn pickup coil of diameter 10 μm , as reported in our recent publications [1, 6, 24]. All the measurements were carried out after cooling a superconducting sample in a magnetic field from 12 K, above T_c , down to 4 K. This minimizes the effect of vortex pinning, which would make it hard to determine the actual vortex distribution. XY scanning of the pickup coil on the sample surface was performed over an area of 100 $\mu\text{m} \times 100$ μm for an 85 μm diameter Pac-Man-shaped plate in 2 μm steps.

In principle, the vortex configuration generated in a sample should be identical regardless of whether or not the sample is cooled in the magnetic field for a pinning-free superconductor. However, for a superconductor with strong pinning centers, the vortex distribution will be quite different depending on whether we cooled the sample in the field or in zero field. We argue that amorphous $\text{Mo}_{80}\text{Ge}_{20}$ thin films deposited under the condition of good cooling are weak-pinning superconductors.

In order to improve the spatial resolution of the vortex images, we not only optimized the distance between the

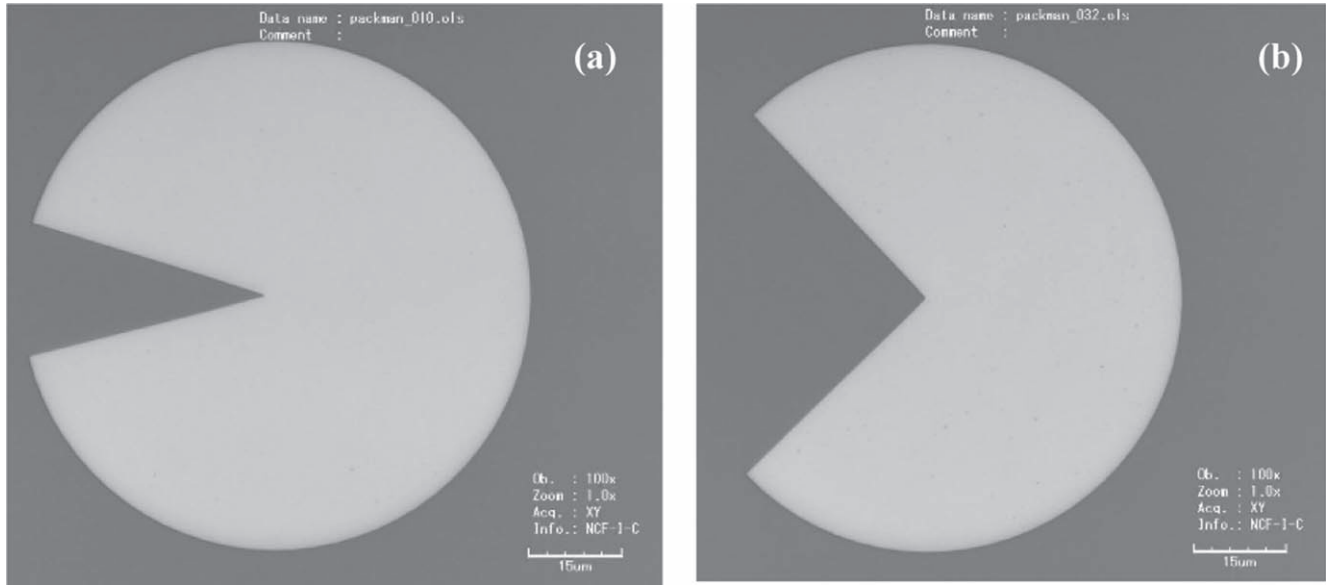


Figure 5. Photographs of Pac-Man-shaped plates prepared by electron-beam lithography and a lift-off technique with a sector defect, of diameter $85\ \mu\text{m}$ and thickness $67\ \text{nm}$ with (a) an opening angle of 30° and (b) an opening angle of 90° .

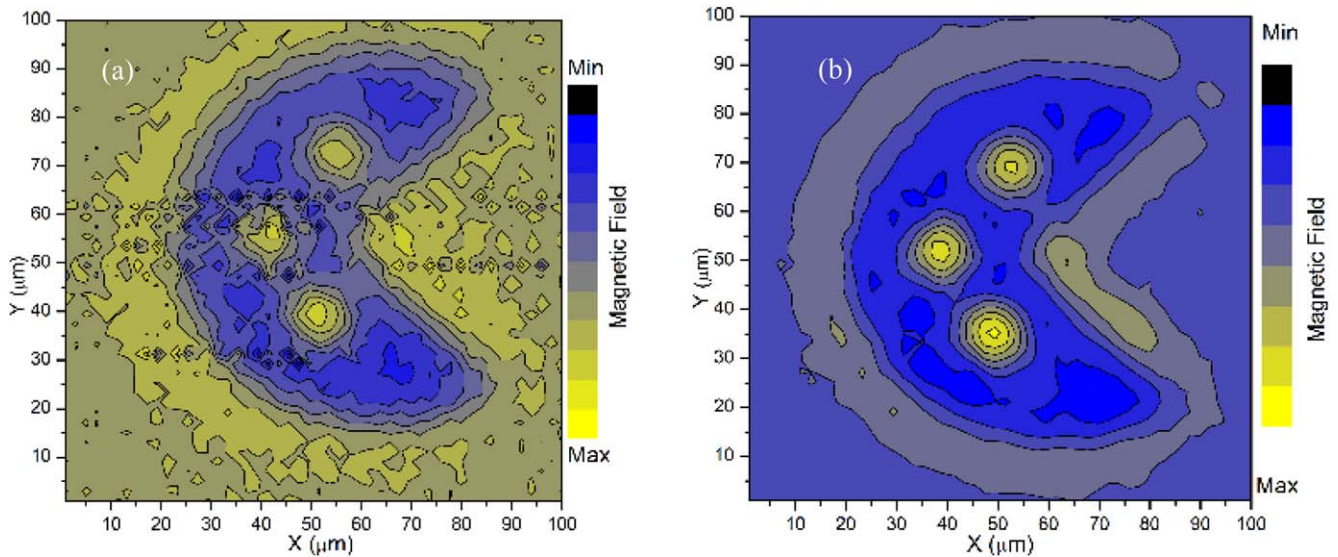


Figure 6. Vortex distributions of a superconducting Pac-Man-shaped plate with a sector defect of opening angle 90° and diameter $85\ \mu\text{m}$. (a) Original image data measured by the SSM. (b) Processed image using our numerical computer program, showing a clearer image.

scanning tip and the sample surface [2, 6] but also upgraded the numerical computer program [27] for observing vortex images such that it corrected for the lift-off distance between the corner tip of the scanning sensor and the sample surface, and the Meissner effect induced by modification of the original magnetic field profile. As noted by Ho *et al* [24], vortices are easily dragged by the superconducting pickup coil during scanning when the height of the pickup coil from the sample surface is less than $1\ \mu\text{m}$. We used an inverse transformation to improve the resolution of the SSM at nano-scales by taking into account the detailed geometry of the pickup (sensor) coil. Smearing the vortex images observed by the SSM can be caused by the following factors: (1) the finite thickness and width of the pickup coil wire, (2) the declined angle of the pickup coil to the sample surface, (3) the distance

between the pickup coil and the sample surface, and (4) perfect diamagnetism of the superconducting pickup coil body. In figure 6, we show a typical example of image processing using software to process the measurement data. We used a superconducting Pac-Man-shaped $\text{Mo}_{80}\text{Ge}_{20}$ plate with an opening angle of 90° and a diameter of $85\ \mu\text{m}$. The image was experimentally taken under the conditions of a step size of $2\ \mu\text{m}$, a separation between the coil and the surface of several μm , an angle between the pickup coil and the sample surface of 7° , and an applied field of $4\ \mu\text{T}$ in the plate. The recovered vortices in the processed image are highlighted as yellow spots in figure 6. A comparison of figures 6(a) and (b) shows that most of the disorders in the experimental image were removed effectively by the computer processing. The Pac-Man-shaped pattern becomes clearer and the sharpness of

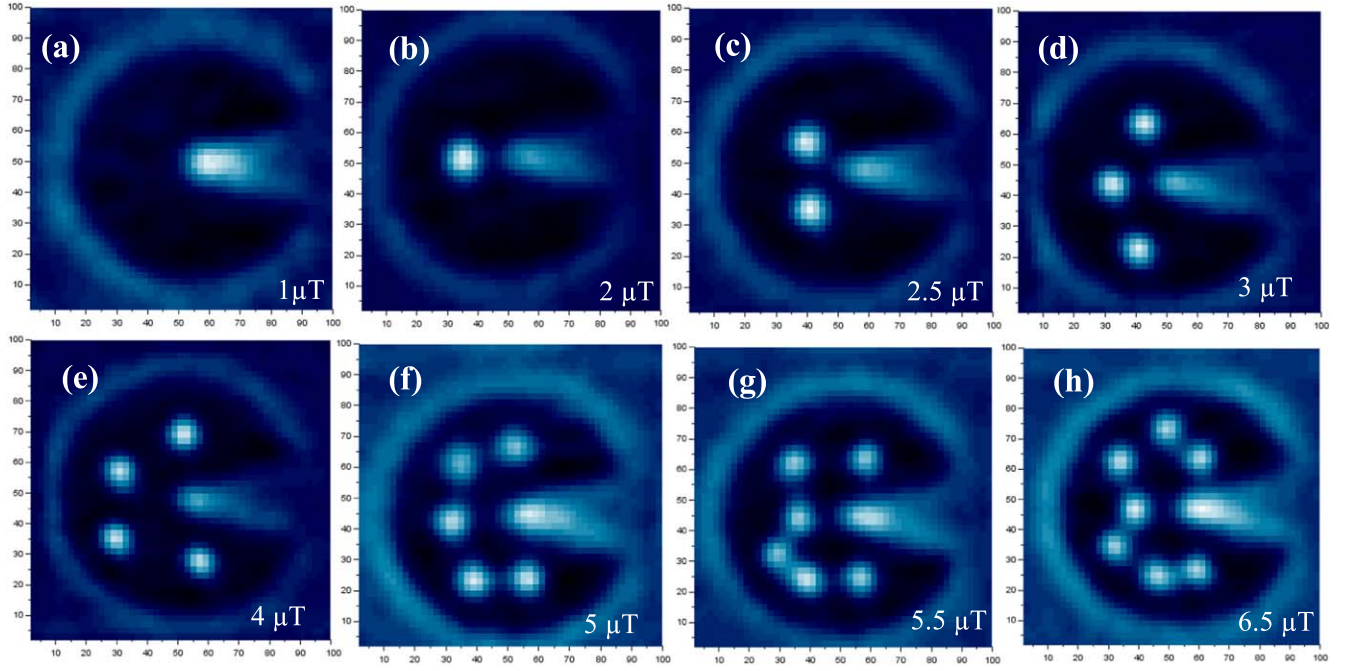


Figure 7. Scanning SQUID microscopy images of *single arc* vortex configurations in a $\text{Mo}_{80}\text{Ge}_{20}$ Pac-Man-shaped plate with diameter $85\ \mu\text{m}$ and opening angle 30° of the defect in several different applied fields at $T = 4\ \text{K}$. The vorticity L is: (a) $L = 0$ at $1\ \mu\text{T}$, (b) $L = 1$ at $2\ \mu\text{T}$, (c) $L = 2$ at $2.5\ \mu\text{T}$, (d) $L = 3$ at $3\ \mu\text{T}$, (e) $L = 4$ at $4\ \mu\text{T}$, (f) $L = 5$ at $5\ \mu\text{T}$, (g) $L = 6$ at $5.5\ \mu\text{T}$, (h) $L = 7$ at $6.5\ \mu\text{T}$.

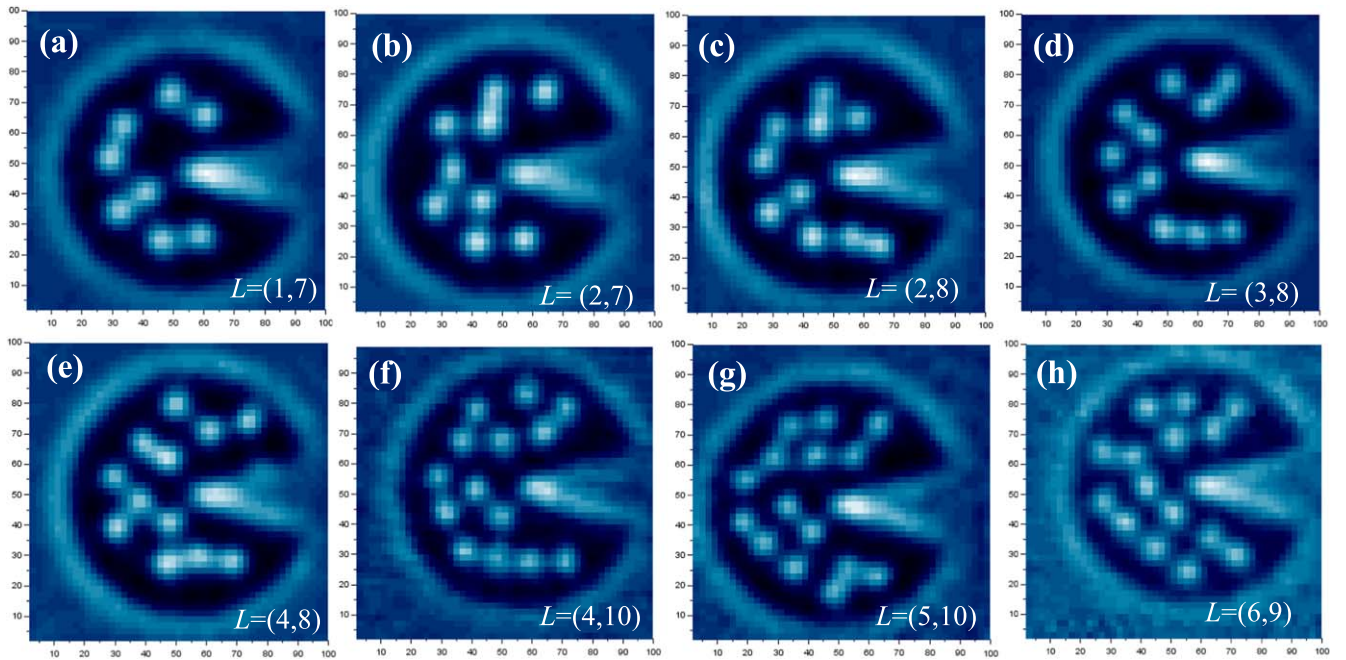


Figure 8. Scanning SQUID microscopy images of vortex distributions in the form of double-arc structures in a $\text{Mo}_{80}\text{Ge}_{20}$ Pac-Man-shaped plate with a diameter $85\ \mu\text{m}$ and an opening angle 30° of the defect in several different applied fields at $T = 4\ \text{K}$. The vorticity L is: (a) $L = (1, 7)$ at $7\ \mu\text{T}$, (b) $L = (2, 7)$ at $8\ \mu\text{T}$, (c) $L = (2, 8)$ at $9\ \mu\text{T}$, (d) $L = (3, 8)$ at $9.5\ \mu\text{T}$, (e) $L = (4, 8)$ at $10\ \mu\text{T}$, (f) $L = (4, 10)$ at $11\ \mu\text{T}$, (g) $L = (5, 10)$ at $12\ \mu\text{T}$, (h) $L = (6, 10)$ at $12.5\ \mu\text{T}$.

the vortex profile is slightly improved from figure 6(a). The diameter of the Pac-Man-shaped plate was similar to the size of the fabricated pattern (figure 5(b)) but appeared to be slightly reduced due to curved magnetic flux lines at the edge

of the pattern. The magnetization distribution on the sample surface becomes clearer and we can distinguish the concentration of the magnetic density around the edge of the pattern.

4. Experimental results

We observed vortex images of $\text{Mo}_{80}\text{Ge}_{20}$ Pac-Man-shaped plates of diameter about $85\ \mu\text{m}$ using an SSM in an external magnetic field up to $14\ \mu\text{T}$. We show our observations in figures 7 and 8, where the XY scales are given in μm units. We explain the vortex distribution evolution with increasing applied magnetic field as follows:

- (1) The Pac-Man-shaped plate remains in the Meissner state in a very weak magnetic field with no vortices in the plate ($L = 0$) (see figure 7(a)). As shown in the figure, the magnetic field is almost repelled from the sample and distributed around the edge of the Pac-Man-shaped plate. Especially, at the tip of the sector defect outside the plate, the magnetic flux lines become dense due to superconducting diamagnetic shielding from the plate. The dense area of magnetic flux can be misidentified as the presence of a vortex. However, it is in fact flux expulsion from the sample surface. As was discussed by Baelus *et al* [17], the energy barrier for vortex penetration into the plate is lowest at the tip of the defect due to a decrease in the local Cooper pair density there. Therefore, as noted by Alstrøm *et al* [22], it becomes easier for vortices to enter the Pac-Man-shaped plate through this defect compared to a perfect disk when the external magnetic field increases. Regarding this, the experimental results are in good agreement with the predictions by numeral calculations.
- (2) As the magnetic field increases, the first vortex penetrates into the Pac-Man-shaped plate ($L = 1$). The vortex was confined strongly by the Meissner state current and repulsion from the defect. Therefore, the single vortex was located at the bisector of the sector defect and surface opposite the tip indent of the defect (see figure 7(b)).
- (3) At $L = 2, 3, 4$, and 5 , respectively figures 7(c)–(f), we found good agreement between the experimental results and the GL calculations. The development of the vortex configuration tends to form a C-shaped arc. As noted by Baelus *et al* [17], with a small defect, the vortex distribution also formed a vortex ring. However, the stable position of the center ring shifted away from the defect. In case of a Pac-Man-shaped pattern, the sector defect is wide enough to expand the ring, modifying the vortex configuration. For $L = 6$ and 7 (see figures 7(g) and (h), respectively), we observed an anomalous vortex configuration, a Σ -shaped form, possibly caused by the presence of weak pinning centers in the sample. Comparing figures 7(g) and (h), we consider that the weakly pinned vortex was located near the tip of the defect. The vortices were also confined by supercurrents, which would push the weakly pinned vortex toward the sector defect tip. This also brought two vortices closer to each other. As the magnetic field increased, one more vortex penetrated at the top of the Pac-Man-shaped plate (see figure 7(h)). The newly

entered vortex tried to form an equilibrium configuration. The bisector line of the sector defect also becomes a line of mirror symmetry in the vortex configuration. The vortex distribution tends to eliminate the influence of the weak pinning to establish a symmetry configuration with the bisector of the defect being the symmetry line. As noted by Kokubo *et al* [2] for a circular disk, the vortex distribution with a pin can form a symmetric line to act as an accidental pin along the symmetry line of the vortex configuration. We recognize that the above discussions are speculative. An alternative explanation for the asymmetric distributions of figures 7(e) and (f) is simply the occurrence of metastable states, even for pin-free samples.

The difference between a Pac-Man-shaped plate and a perfect disk can be explained by the difference in the degrees of freedom with respect to the sector defect. A Pac-Man-shaped plate has only one mirror-symmetry line. It is easy to adapt the vortex configuration of a perfect disk with infinite lines of symmetry to one mirror-symmetry line. Figure 8 shows that vortex images exhibit a two-arc structure for $L > 7$ on the same pattern. The maximum number of vortices in an arc for a Pac-Man-shaped plate with an opening angle of 30° was complicated to determine in the experimental images because a possible weak pin accommodate a vortex near the tip of the sector defect. However, it is in the range from seven of figure 7(h) to eight of figure 8(a), as confirmed by the predictions of GL calculations. When the vorticity increases to $L = 8$, one vortex penetrates near the tip indent of the defect and the seven other vortices formed a C-shaped pattern as one arc. Using the standard notation, this is a double-arc structure $L = (1, 7)$. We found that the outer arc of figure 8(a) has the same vorticity of seven as the single-arc configuration of figure 7(h), but the Σ -shaped pattern of figure 7(h) becomes a C-shaped structure in the outer arc of the double arcs of figure 8(a). We believe that the vortex distribution is modified by the repulsion of the inner vortex and a possible weak pin, which might be located along the bisector of the defect. The interactions between the inner and outer vortices were more visible for $L = (2, 7)$, which was generated by adding one more vortex in the inner arc. The vortex–vortex interaction in the inner arc placed a vortex of the inner arc on the symmetry line. When the vortex populations become crowded as the vorticity increases, the possible weak pin becomes less effective in pinning the vortex because the vortex–vortex repulsion becomes more dominant in determining the distribution at higher vorticities at $L = (2, 8)$, $(3, 8)$, $(4, 8)$, $(4, 10)$, $(5, 10)$, $(6, 9)$, as respectively shown in figures 8(c)–(h). We found that the vortex distribution tends to duplicate the pattern formation of a single vortex configuration in the evolution of the outer-arc vorticity under the influence of the inner-arc vortices. The development of the inner vortex at figures 8(c) and (d), we found that the symmetry line of the inner arc is different from the bisector of the sector defect. However, as the inner vorticity increased, the geometrical symmetry line in the vortex distribution was recovered. For example, in figures 8(e)–(f), the addition of a

vortex at the bottom of the inner arc changed the direction of the symmetry line of the vortex configuration to be closer to being parallel to the bisector line of the defect. Similarly, by further increasing the applied magnetic field, one more vortex penetrates at the bottom of the inner-arc configuration while the mirror-symmetry line of the inner vortex configuration is almost parallel to the geometrical symmetry line of the Pac-Man-shaped plate. It seems to be preferential for the vortices to have a configuration in good accordance with the sample geometry with regard to symmetry. For example, figures 8(a)–(h) have the same vorticity in the outer arc but a different distribution due to the different inner-arc vorticity, though they always tend towards an equilibrium configuration so that the bisector line of the defect becomes a common mirror-symmetry line.

We consider that the addition of a sector defect in a disk strongly modifies the distribution of vortices. For example, a Pac-Man-shaped plate forms a trapezoid pattern with a vorticity of four, as shown in figure 7(e), while the configuration of vortices in a circular disk is known to have a square pattern [2, 24]. In table 2, we list the vortex configurations of our Pac-Man-shaped plates along with those for a circular disk and a square plate. Table 2 shows that a Pac-Man-shaped plate exhibits a similar vorticity for multiple layers as a perfect disk. However, the positions of the vortices in the distribution are quite different. As noted by Grigorieva *et al* [12] and Kokubo *et al* [2], the outer shell is composed of a ring of vortices while the inner shell forms a triangle for $L = (3, 8)$ in a circular disk, while the vortices in the Pac-Man-shaped plate consist of an outer and inner arc. We notice that the two ‘lips’ of the Pac-Man mouth, or the corners of the pattern, almost never accommodate vortices (see figure 8). The distribution of the external magnetic field is lowest at the corners and, therefore, the chance of field penetration is the lowest there. Also, the presence of the defect tends to encourage the vortices to interact with the boundary supercurrents, pushing the arc area towards the circular arc side opposite to the sector defect [17], away from the corners.

5. Summary

We reported systematic theoretical and experimental investigations of the vortex configurations in a mesoscopic superconducting circle plate with a sector defect. Our theoretical predictions were generally in good agreement with the experimental results obtained for an amorphous $\text{Mo}_{80}\text{Ge}_{20}$ Pac-Man-shaped plate of $85\text{ }\mu\text{m}$ diameter. They share the general features of vortex configuration, including the filling rule into arc structures. We also found that the critical vorticity (magic number) of a single arc in the Pac-Man-shaped plate depends on the opening angle of the sector defect. We presented how the symmetry breaking of the circular disk influences the vortex distribution by the presence of the sector defect. The vortex configuration of the Pac-Man-shaped plate shares its mirror-symmetry line with the bisector line of the sector defect. This is not the case for the vortex distribution of a circular disk

with infinite degrees of rotational freedom. The vortex configuration of the Pac-Man-shaped plate forms a unique symmetric structure with respect to the bisector line of the defect and the mirror-symmetry line of the mesoscopic Pac-Man-shaped system plays an important role in generating a non-trivial distribution of vortices with mirror symmetry, as revealed both experimentally and theoretically. Of particular interest is the magic number in the Pac-Man-shaped disk for vortex filling. We discovered that the inner arc fills up to the magic number before a higher multiple arc appears. The magic number can be controlled by tuning the opening angle of the defect, while the magic number is fixed for a circular disk, square plate, and other regular polygons. By comparing the free energies of the vortex distributions obtained by numerical simulations, we found that the ratio of the outer-arc vorticity to the inner-arc vorticity is approximately two when the double arcs are fully occupied by vortices. This is influenced by the presence of various metastable vortex configurations observed in the numerical simulations. The experimental observations do not always match the most stable states of the superconducting system. The metastable states were often observed among the many measurement trials. However, we found good agreement between the experimental observations using the scanning SQUID microscope and the vortex configurations obtained by the GL calculations. An interesting feature of the vortex configurations is that the distributions of vortices do not always form a symmetric configuration under the influence of possible weak pins at the earlier stages of the vortex penetration. However, further evolution of the vortex configuration always tends to accommodate a new vortex in a well-balanced position with regard to the mirror-symmetry line of the sector defect. The repulsive interaction between the physical phenomena around the defect and vortices tends to expand the area of the vortex distribution toward the surrounding area away from the defect. We consider that this is why the magic number of the inner-arc vorticity for an opening angle of 30° is larger than that of a circular disk. Increasing the opening angle reduces the superconducting area for the same diameter, and yields a lower magic number, as revealed for the opening angle of 90° . We developed software to improve the resolution of the experimental images by accounting for the practical problems of a scanning SQUID microscope, such as the structure of the pick coil, the scanning process and environment conditions.

Acknowledgments

This work was partially supported by a Grant-in-Aid from the Japan Society for the Promotion of Science (JSPS) (No. 25600018, No. 26820130, No. 26800192, No. 23226019, No. 15K13979).

ORCID iDs

Masahiko Hayashi  <https://orcid.org/0000-0002-6693-8881>
Takekazu Ishida  <https://orcid.org/0000-0002-9629-5178>

References

- [1] Huy H T, Kato M and Ishida T 2013 *Supercond. Sci. Technol.* **26** 065001
- [2] Kokubo N, Okayasu S, Kanda A and Shinozaki B 2010 *Phys. Rev. B* **82** 014501
- [3] Kokubo N, Okayasu S, Nojima T, Tamochi H and Shinozaki B 2014 *J. Phys. Soc. Japan* **83** 083704
- [4] Baelus B J, Peeters F M and Schweigert V A 2000 *Phys. Rev. B* **61** 9734
- [5] Zhao H J, Misko V R, Peeters F M, Oboznov V, Dubonos S V and Grigorieva I V 2008 *Phys. Rev. B* **78** 104517
- [6] Huy H T, Shishido H, Hayashi M, Yotsuya T, Kato M and Ishida T 2013 *Physica C* **484** 86
- [7] Cabral L R E and Aguiar J A 2007 *Physica C* **460–462** 1295
- [8] Cabral L R E and Aguiar J A 2008 *Physica C* **468** 722
- [9] Cabral L R E and Aguiar J A 2009 *Phys. Rev. B* **80** 214533
- [10] Chibotaru L F, Ceulemans A, Bruyndoncx V and Moshchalkov V V 2000 *Nature* **408** 83
- [11] Pereira P J, Chibotaru L F and Moshchalkov V V 2011 *Phys. Rev. B* **84** 144504
- [12] Grigorieva I V, Escoffier W, Richardson J, Vinnikov L Y, Dubonos S and Oboznov V 2006 *Phys. Rev. Lett.* **96** 077005
- [13] Matsumoto H, Huy H T, Miyoshi H, Okamoto T, Vu T D, Kato M and Ishida T 2016 *Physica C* **530** 46
- [14] Vu T D, Huy H T, Matsumoto H, Miyoshi H, Miyajima S, Shishido H, Kato M and Ishida T 2016 *Phys. Proc.* **81** 93
- [15] Bean C P and Livingston J D 1964 *Phys. Rev. Lett.* **12** 14
- [16] de Gennes P G 1999 *Superconductivity in Metals and Alloys* 1st edn (New York: Perseus Books)
- [17] Baelus B J, Kadowaki K and Peeters F M 2005 *Phys. Rev. B* **71** 024514
- [18] Grigorieva I V, Escoffier W, Misko V R, Baelus B J, Peeters F M, Vinnikov L Y and Dubonos S V 2007 *Phys. Rev. Lett.* **99** 147003
- [19] Clem J R J R 1974 *Low Temperature Physics* ed K D Timmerhaus, W J Sullivan and E F Hammel vol 3 (New York: Plenum) p 102
- [20] Geim A K, Dubonos S V, Grigorieva I V, Novoselov K S, Peeters F M and Schweigert V A 2000 *Nature* **407** 55
- [21] Zhao H J, Misko V R, Peeters F M, Dubonos S, Oboznov V and Grigorieva I V 2008 *Europhys. Lett.* **83** 17008
- [22] Alstrøm T S, Sørensen M P, Pedersen N F and Madsen S 2010 *Acta Applicandae Mathematicae* **115** 63
- [23] Kato M and Fujibayashi D E 2013 *Phys. Proc.* **45** 133
- [24] Huy H T, Kato M, Sato O, Hayashi M, Yotsuya T and Ishida T 2013 *Physica C* **494** 99
- [25] Braverman G M, Gredeskul S A and Avishai Y 1999 *Phys. Rev. B* **59** 12039
- [26] Pearl J 1964 *Appl. Phys. Lett.* **5** 65
- [27] Hayashi M, Ebisawa H, Huy H T and Ishida T 2012 *Appl. Phys. Lett.* **100** 182601